Mass transfer towards a reactive particle in a fluid flow: Numerical simulations and modeling

Mostafa Sulaiman [a], Eric Climent [b,*], Abdelkader Hammouti [a], Anthony Wachs [c,d]

[a] IFP Énergies Nouvelles, Fluid Mechanics Department, Rond-point de l'échangeur de Solaize, BP 3, 69360 Solaize, France
[b] Institut de Mécanique des Fluides de Toulouse (IMFT), Université de Toulouse, CNRS, Toulouse, France
[c] Department of Mathematics, University of British Columbia, 1984 Mathematics Road, Vancouver, BC V6T 1Z2, Canada
[d] Department of Chemical and Biological Engineering, University of British Columbia, 2360 East Mall, Vancouver, BC V6T 1Z3, Canada

HIGHLIGHTS

- Model for the mass transfer coefficient accounting for diffusion and internal first order chemical reaction.
- Direct numerical simulations (DNS).
- Wide range of Reynolds and Schmidt numbers and Thiele modulus.
- Reactive Sherwood number.

GRAPHICAL ABSTRACT

Keywords:
Catalyst particle
Mass transfer
Sherwood number
Chemical reaction
Thiele modulus
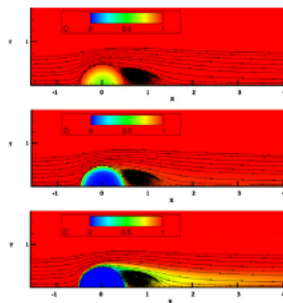
ABSTRACT

We study mass transfer towards a solid spherical catalyst particle experiencing a first order irreversible reaction coupled to an external laminar flow. Internal chemical reaction and convective diffusive mass transfer in the surrounding fluid flow are coupled by concentration and flux boundary conditions at the particle surface. Through this coupling, the mean particle surface and volume concentrations are predicted and the internal/external Sherwood numbers are obtained. We investigate the interplay between convection, diffusion, and reaction by computational fluid dynamics and establish a model for the mass transfer coefficient accounting for diffusion and internal first order chemical reaction. We obtain a prediction of the mass transfer coefficient through mass balance or using the classical additivity rule. The model is numerically validated by fully resolved numerical simulations over a wide range of Reynolds number, Schmidt number and Thiele modulus which shows that assuming decoupled treatment of external and internal mass transfer gives very accurate predictions. Finally, we test the unsteady response of the model. The model predicts the evolution of the mean volume concentration for a particle placed in a steady convective diffusive stream. Predictions of the unsteady model are in very good agreement with computed results.

1. Introduction

1.1. Industrial context

Interactions of solid and fluid phases are prominent in a wide range of industrial chemical engineering applications of energy or raw material transformation. While the two phases are in contact, mass transfer occurs between them. In petrochemical processes, fluid solid interactions occur in fluidized and fixed bed reactors that are used for catalytic cracking of large scale basic compounds into desirable molecules, that can be used as fuel for engines (Jarullah et al., 2017). Different modes of mass transfer take place in these systems. When a liquid or a gas flows through a randomly stacked batch of solid catalytic particles, referred to as

* Corresponding author.
E-mail address: ecliment@imft.fr (E. Climent).

a fixed bed, or through fine catalytic particles maintained in a fluidized state, referred to as a fluidized bed, adsorption and diffusion in zeolite material occur. Molecules exchange takes place at the zeolite matrix interface and diffusion in meso and macro pores. In these systems, reactants are usually transferred from the continuous "bulk" phase to the dispersed phase where a chemical reaction takes place in the form of a heterogeneously catalyzed gas or liquid reaction (Rossetti, 2017), within the catalyst particles. Biomass gasification processes also represent an active engineering field for solid fluid interactions. These processes aim at extracting liquid bio fuel from abundant organic material through pyrolysis. They are usually operated in fluidized bed gasifiers (Ismail et al., 2017; Neves et al., 2017) or fixed bed gasifiers (Baruah et al., 2017; Mikulandrić et al., 2016) where solid biomass particles undergo complex mass transfer enhanced by chemical reaction, coupled to heat transfer and hydrodynamics. The strong mass transfer experienced by the solid particle is associated with conversion that occurs through phase change leading to severe particle deformations. The same interactions are encountered in many other industrial applications. Modeling the interaction between solid and fluid phases, and the interplay among fluid flow, heat and mass transfer with chemical reaction, is of tremendous importance for the design, operation and optimization of all the afore mentioned industrial operating systems. Investigating mass transfer coefficients between the dispersed solid phase and the continuous fluid phase at the particle scale, referred to as micro scale, where the interplay between the two phases is fully resolved, helps to propose closure laws which can be used to improve the accuracy of large scale models through multi scale analysis.

1.2. Literature overview

Many studies have been carried out to analyze and model coupling phenomena in particulate flow systems. For dilute regimes, Ranz and Marshall (1952), Clift et al. (2005), Whitaker (1972) and more recently (Feng and Michaelides, 2000) have carried out studies to characterize the coupling of mass/heat transfer with hydrodynamics for a single spherical particle. This configuration is characterized by the Reynolds number for the flow regime and the Schmidt number (ratio of momentum to molecular diffusion coefficients). They established correlations for the Sherwood number in diffusive convective regimes in the absence of chemical reaction for an isolated particle. For dense regimes, Gunn (1978) measured the heat transfer coefficient within a fixed bed of particles including the effect of the particulate volume concentration. Piché et al. (2001) and Wakao and Funazkri (1978) investigated mass transfer coefficients in packed beds for different applications.

There has also been a considerable interest in systems incorporating chemical reaction. Sherwood and Wei (1957) studied experimentally the mass transfer in two phase flow in the presence of slow irreversible reaction. Ruckenstein et al. (1971) studied unsteady mass transfer with chemical reaction and deduced analytical expressions for transient and steady state average Sherwood numbers for bubbles and drops. This has been extended to the case of a rising bubble under creeping flow assumptions (Pigeonneau et al., 2014). Losey et al. (2001) measured mass transfer coefficient for gas liquid absorption in the presence of chemical reaction for a packed bed reactor loaded with catalytic particles. Kleinman and Reed (1995) proposed a theoretical prediction of the Sherwood number for coupled interphase mass transfer undergoing a first order reaction in the diffusive regime. For a solid spherical particle experiencing first order irreversible reaction in a fluid flow, Juncu (2001) and Juncu (2002) investigated the unsteady conjugate mass transfer under creeping flow assumption. The effect of Henry's law and diffusion coefficient ratio on the Sherwood number were investigated when the chemical reaction is occurring either in the dispersed or continuous phases. Lu et al. (2018) employed an Immersed Boundary Method (IBM) to study mass transfer with a first order irreversible surface chemical reaction and applied it to a single stationary sphere under forced convection. The external mass transfer coefficients were numerically computed and compared to those derived from the empirical correlation of Frössling. Wehinger et al. (2017) also performed numerical simulations for a single catalyst sphere with three pore models with different complexities: instantaneous diffusion, effectiveness factor approach and three dimensional reaction diffusion where chemical reaction takes place only within a boundary layer at the particle surface. In Partopour and Dixon (2017b), a computational approach for the reconstruction and evaluation of the micro scale catalytic structure is employed to perform a pore resolved simulations coupled with the flow simulations. Dierich et al. (2018) introduced a numerical method to track the interface of reacting char particle in gasification processes. Dixon et al. (2010) modeled transport and reaction within catalyst particles coupled to external 3D flow configuration in packed tubes. Through this method, 3D temperature and species fields were obtained. Bohn et al. (2012) studied gas solid reactions by means of a lattice Boltzmann method. Effectiveness factor for diffusion reaction within a single particle was compared to analytical solutions and the shrinkage of single particle was quantitatively compared experiments.

In this paper, our efforts are devoted to the coupling of a first order irreversible reaction taking place within a solid catalyst particle experiencing internal diffusion and placed in a flow stream (external convection and diffusion). In order to fully understand the interplay between convection, diffusion and chemical reaction we have carried out fully coupled direct numerical simulations to validate a model which predicts the evolution of the Sherwood number accounting for all transport phenomena. The paper is organized as follows. First, we investigate the diffusive regime and then include external convection. The prediction of the mass transfer coefficient is validated through numerical simulations over a wide range of dimensionless parameters. Finally, the model is tested under unsteady conditions.

2. Diffusive regime

2.1. Internal diffusion and reaction

We consider a porous catalyst spherical bead of diameter d_p^* $2r_p^*$, effective diffusivity D_s^* within the particle, and effective reactivity k_s^*. Please note that dimensional quantities are distinguished from dimensionless quantities by a "*" superscript. A reactant is being transferred from the surrounding fluid phase to the solid phase, where it undergoes a first order irreversible reaction. We use the term effective for the molecular diffusion and reaction constant of the kinetics because these quantities are related to the internal microstructure of the porous media (porosity, tortuosity and specific area for the catalytic reaction). We assume that this can be approximated by a continuous model in which the effective diffusion coefficient is typically ten to hundred times lower than in unconfined environment (diffusion coefficient is D_f^* outside the particle). The constant k_s^* of a first order irreversible chemical reaction is also assumed constant due to homogeneous distribution of the specific area within the porous media experiencing the catalytic reaction. The particle is immersed in an unbounded quiescent fluid of density ρ_f^* and viscosity μ_f^*. Based on these assumptions, we can write the balance equation for the reactant of molar concentration C^* in the solid phase:

$$\frac{\partial C^*}{\partial t^*} \quad D_s^* \nabla^2 C^* \quad k_s^* C^* \tag{1}$$

At steady state, the concentration profile inside the catalyst particle can be found by integrating Eq. (1) and using two boundary conditions, shortly summarized: $C^* = C_s^*|_{r^* = r_p^*}$ and $dC^*/dr^* = 0|_{r^* = 0}$. The solution is available in transport phenomena textbooks such as Bird et al. (2015):

$$C_r = \frac{C^*}{C_s^*} = \frac{\sinh(\phi r)}{2r \, \sinh(\phi/2)} \tag{2}$$

where $r = r^*/d_p^*$ is the dimensionless radial position, C_s^* the surface concentration, and $\phi = d_p^* \sqrt{\frac{k_s^*}{D_s^*}}$ is the Thiele modulus.

The dimensional mass flux density at the particle surface $r^* = r_p^*$ can be found by deriving Eq. (2) with respect to r^* and inserting it in Eq. (3):

$$N_S^* = -D_s^* \frac{dC^*}{dr^*}\Big|_{r^* = r_p^*} = \frac{D_s^* C_s^*}{d_p^*}\left(\frac{\phi}{tanh(\phi/2)} - 2\right) \tag{3}$$

The effectiveness factor η (Eq. (4)) for a catalyst particle is defined as the internal rate of reaction inside the particle, to the rate that would be attained if there were no internal transfer limitations. For a catalyst bead of given surface concentration C_s^*, the effectiveness factor is:

$$\eta = \frac{6}{\phi}\left(\frac{1}{tanh(\phi/2)} - \frac{2}{\phi}\right) \tag{4}$$

2.2. Particle surface concentration with external diffusion

Assuming a purely diffusive regime, mass transfer in the fluid phase is governed by the following equation:

$$\frac{\partial C^*}{\partial t^*} = D_f^* \nabla^2 C^* \tag{5}$$

The concentration profile in the fluid phase can be found through integrating Eq. (5), at steady state, with two Dirichlet boundary conditions, $C^*|_{r^* = r_p^*} = C_s^*$ and $C^*|_{r = \infty} = C_\infty^*$. We aim in this section at finding the particle surface concentration at steady state. Once the surface concentration is known, the external concentration gradient between the particle surface and the bulk can be found. Also, the mean volume concentration of the particle can be evaluated, which will then permit to evaluate the internal and external Sherwood numbers as a measure of dimensionless mass transfer.

The external diffusive problem can be coupled to the internal diffusive reactive problem through two boundary conditions at the solid fluid interface: (i) continuity of mass flux and (ii) continuity of concentration. At steady state, a balance is reached between diffusion from the fluid phase and consumption due to internal reaction in the solid particle, resulting in a specific (unknown) concentration C_s at the particle surface. The flux density within the fluid film surrounding the particle can be written as:

$$N_f^* = k_f^*(C_s^* - C_\infty^*) \tag{6}$$

which is equal to the flux density through the solid surface Eq. (3), yielding:

$$k_f^*(C_s^* - C_\infty^*) = D_s^* \frac{C_s^*}{d_p^*}\left(\frac{\phi}{tanh(\phi/2)} - 2\right) \tag{7}$$

k_f^* represents the mass transfer coefficient in the fluid phase which can be obtained from the Sherwood number $Sh = k_f^* d_p^*/D_f^*$. Then we can determine the surface concentration as:

$$C_s^* = \frac{C_\infty^*}{1 + \frac{1}{Bi}\left(\frac{\phi/2}{tanh(\phi/2)} - 1\right)} \tag{8}$$

where $Bi = k_f^* d_p^*/2D_s^*$ is the mass transfer Biot number. The external mass transfer coefficient $k_f^* = 2D_f^*/d_p^*$ defined in (6) is obtained analytically from Fick's law applied to the steady profile of external diffusion in an infinite domain, $C^*(r) = (C_s^* - C_\infty^*)\frac{r_p^*}{r^*} + C_\infty^*$. For this configuration, the surface concentration is prescribed analytically as follows:

$$C_s^* = \frac{C_\infty^*}{1 + \gamma\left(\frac{\phi/2}{tanh(\phi/2)} - 1\right)} \tag{9}$$

which explicitly depends on the kinetics of the chemical reaction. The dimensionless numbers governing the problem, in the absence of convection in fluid phase, are the Thiele modulus ϕ and the diffusion coefficient ratio $\gamma = \frac{D_s^*}{D_f^*}$.

2.3. General model including convection effects

When the particle is experiencing an external convective stream, no analytical solution can be deduced for the surface concentration due to the inhomogeneity of the velocity and concentration fields. Similarly to the diffusion reaction problem presented in the first case, where the Sherwood number was evaluated analytically, it will be instead evaluated from one of the correlations established for convective diffusive problems by Feng and Michaelides (2000), Whitaker (1972) and Ranz and Marshall (1952)). According to this, the mean surface concentration $\overline{C_s^*}$ can be obtained.

In a general case, the molar flux towards the particle surface (Eq. (6)) can be written as:

$$N_f^* = Sh \frac{D_f^*}{d_p^*}\left(\overline{C_s^*} - C_\infty^*\right) \tag{10}$$

which under steady state conditions is equal to the consumption rate in the particle

$$N_f^* = \frac{d_p^*}{6}\eta k_s^* \overline{C_s^*} \tag{11}$$

where η is the effectiveness factor Eq. (4). The internal reaction changes only the concentration gradient inside the particle, and thus, does not change the value of the external Sherwood number. We assume that the concentration over the particle surface is equal to its average $\overline{C_s^*}$.

This gives the general expression for the surface concentration

$$\overline{C_s^*} = \frac{C_\infty^*}{1 + \frac{2\gamma}{Sh}\left(\frac{\phi/2}{tanh(\phi/2)} - 1\right)} \tag{12}$$

and the molar flux

$$N_f^* = \frac{C_\infty^*}{\frac{d_p^*}{D_f^* Sh} + \frac{6}{d_p^* \eta k_s^*}} \tag{13}$$

where the Sherwood number Sh is a function of the Reynolds number $Re = \rho_f^* u_{ref}^* d_p^*/\mu_f^*$ and the Schmidt number $Sc = \mu_f^*/\rho_f^* D_f^*$, and u_{ref}^* is a characteristic velocity scale. Sh is equal to 2 for pure diffusion in the fluid recovering Eq. (9).

3. Transfer/reaction in presence of a fluid flow

3.1. Numerical simulations

We define the full flow domain as Ω, the part of Ω occupied by the solid particle as P and the part of Ω occupied by the fluid as $\Omega \setminus P$. The whole numerical problem involves solving the

Navier Stokes Eqs. (14) and (15) under the no slip boundary condition at the particle surface $r^* = r_p^*$ together with the mass balance equations in the solid (16) and in the fluid (17) submitted to the continuity of the concentration and the continuity of the mass flux at the particle surface ∂P defined by $r^* = r_p^*$, i.e., $C_{r_p^{*+}}^* = C_{r_p^*}^*$ and $D_f^* \frac{dC}{dr}|_{r_p^{*+}} = D_s^* \frac{dC^*}{dr}|_{r_p^*}$, respectively. A uniform flow $u_{in}^* = u_{ref}^*$ and a constant concentration are imposed at the inlet of the domain. The free stream and symmetry conditions simply state that the normal velocity, the tangential stress, and the mass flux are zero on the boundary under consideration. The outflow condition allows the flow to leave the domain without significantly perturbing the computed field.

$$\nabla \cdot \mathbf{u}^* = 0, \quad \text{in} \quad \Omega \backslash P \tag{14}$$

$$\rho_f^* \frac{D\mathbf{u}^*}{Dt^*} = \nabla p^* + \mu \nabla^2 \mathbf{u}^*, \quad \text{in} \quad \Omega \backslash P \tag{15}$$

$$\frac{\partial C^*}{\partial t^*} = D_s^* \nabla^2 C^* = k_s^* C^*, \quad \text{in} \quad P \tag{16}$$

$$\frac{\partial C^*}{\partial t^*} + \mathbf{u}^* \cdot \nabla C^* = D_f^* \nabla^2 C^*, \quad \text{in} \quad \Omega \backslash P \tag{17}$$

First, the Navier Stokes equations are solved to reach steady state for the desired Reynolds number. Then Eqs. (16) and (17) only are solved to determine the temporal evolution of the concentration. Starting from the initial conditions $C^* = 0$ in the particle and $C^* = C_\infty^*$ in the fluid, the conjugate problem is solved using the JADIM code developed in our group.

The basic numerical methods used in this code have been thoroughly described by Magnaudet et al. (1995) and Calmet and Magnaudet (1997). Consequently they will be only quickly summarized here. The JADIM code solves the incompressible Navier Stokes equations and the concentration equation in general orthogonal curvilinear coordinates. Equations are integrated in space using a finite volume method in which advective and diffusive terms are evaluated with second order centered schemes. The solution is advanced in time by means of a three step Runge Kutta time stepping procedure where the nonlinear terms are computed explicitly while the diffusive terms are treated using the semi implicit Crank Nicholson algorithm. Incompressibility is satisfied after the third intermediate time step by solving a Poisson equation for an auxiliary potential from which the true pressure is deduced. The complete algorithm is second order accurate in both space and time.

The orthogonal mesh grid used in the present work is presented in Fig. 1. The orthogonal axi symmetric mapping is obtained by using the streamlines and the equipotential lines of the potential flow around a circular cylinder. The mesh is stretched in order to enforce at least four points in the external mass boundary layer thickness that scales as $Pe^{-1/3}$ ($Pe = Re.Sc$ is the Peclet number). Simulations are carried out under a 2D axi symmetric configuration which reproduces the geometry of a spherical particle. The fluid computational domain is limited by the particle surface and by external boundaries on which inflow, free stream, axial symmetry, and outflow boundary conditions are imposed, respectively. The equations are solved inside the particle over a polar mesh adjusted to the fluid mesh at the particle surface. The internal mass boundary layer thickness gets thinner when the kinetics of the chemical reaction increases. The mesh is then refined following the scaling of the internal boundary layer as ϕ^{-1}. At least four grid points stand within the internal boundary layer in order to compute properly the interface gradient of concentration. A particle of radius r_p is placed in domain with a spatial extension of at least $r_\infty^* = 100 r_p^*$, so that the assumption of infinite domain is physically valid.

3.1.1. Validation of internal diffusion reaction

The numerical method has been validated in case of diffusion reaction inside the particle. The surface concentration has been fixed, $C_s^* = 1$, and the concentration profiles have been compared at steady state to those of the analytical solution for different values of Thiele moduli, representing slow, intermediate, and fast reaction rates. The numerical results show a very good agreement in Fig. 2 with the analytical solution, Eq. (2).

3.1.2. Validation of external convection diffusion

The numerical method is firstly validated through the comparison of computed Sherwood numbers with existing correlations in a convective diffusive problem without reaction. A spherical particle is placed at the center of a 2D axi symmetric domain, Fig. 1, of
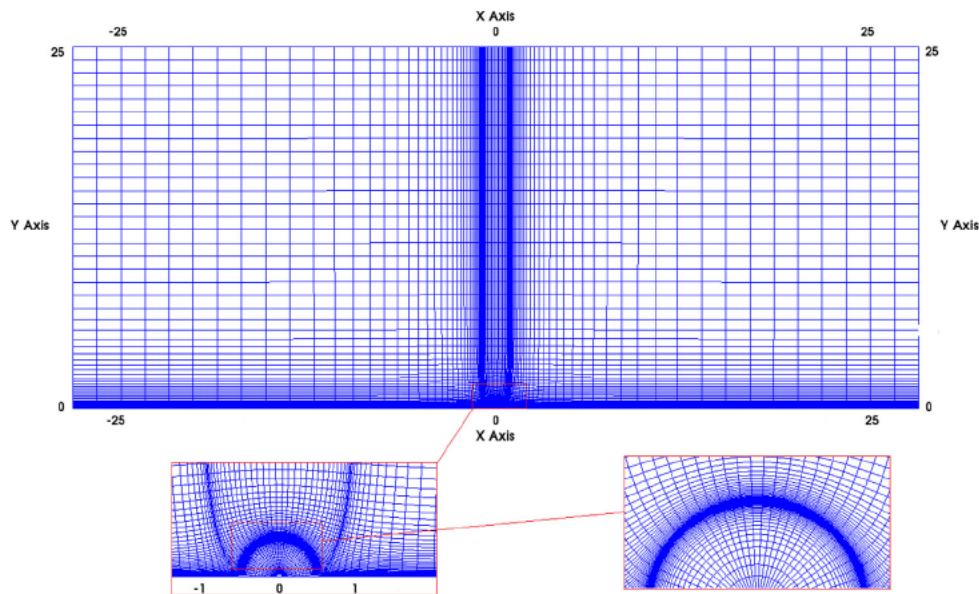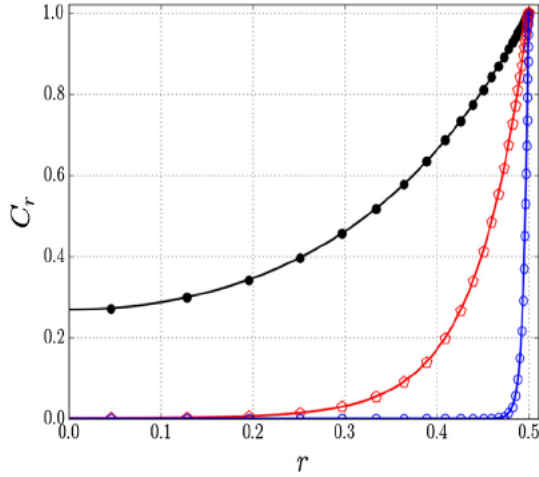

Fig. 1. Domain geometry and mesh grid.

Fig. 2. Concentration profiles: comparison of simulations with analytical solution for different Thiele moduli. Analytical solution is represented by continuous lines and numerical simulations is represented by markers. Black line and black filled circles correspond to $\phi^2 = 40$. Red line and open red pentagons correspond to $\phi^2 = 4 \cdot 10^2$. Blue line and opened circles correspond to $\phi^2 = 4 \cdot 10^3$. (For interpretation of the references to color in this figure legend, the reader is referred to the web version of this article.)
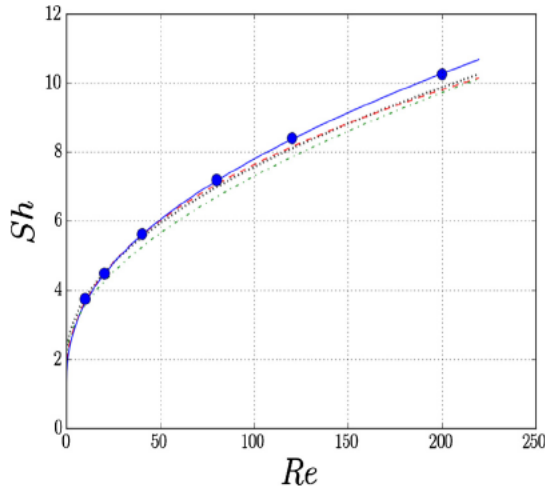

Fig. 3. Sherwood number comparison with previous references for Schmidt number $Sc = 1$. Numerical results are represented by filled blue circles. The blue continuous line stands for the correlation of Feng and Michaelides (2000), doted line for the correlation of Ranz and Marshall (1952), dashed-doted line for the correlation of Whitaker (1972) and dashed line for the correlation of Clift et al. (2005). (For interpretation of the references to color in this figure legend, the reader is referred to the web version of this article.)

dimensions $L_x^* = L_y^* = L_z^* = 100 r_p^*$. A constant inlet velocity is imposed with constant concentration $C_\infty^* = 0$ and a constant concentration $C_s^* = 1$ is imposed at the particle surface. The Sherwood number $Sh = \frac{k_f^* d_p^*}{D_f^*}$ is evaluated at steady state and compared with the reference correlations for Reynolds numbers ranging from diffusive regime to $Re = 200$. We chose the highest value of $Re = 200$ so that the flow remains 2D axi symmetric. Beyond this regime, we would need to verify the validity of the model with 3D simulations. Our computed Sherwood numbers are in a very good agreement with those of Feng and Michaelides (2000) and are shown in Fig. 3.

3.1.3. Diffusion reaction: internal/external coupling

The analytical solution for the mean surface concentration found in Eq. (9) is compared to the simulation results. In a finite
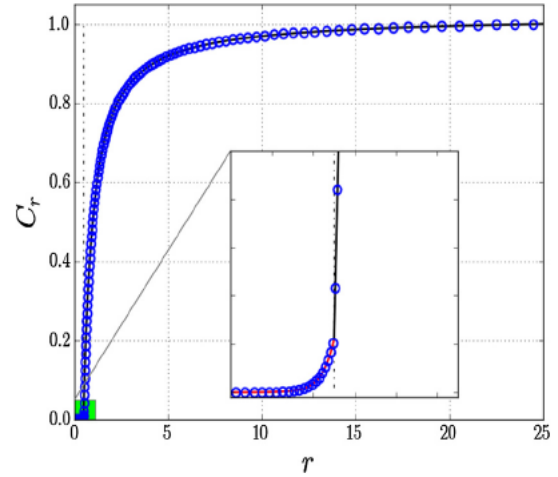

Fig. 4. Concentration profile as function of dimensionless radius for $\gamma = 10$ and $\phi = 20$. Inset stands for a zoom on the particle surface ($r^*/r_p^* = 1$). Particle interface is represented by vertical dashed-doted line, analytical solution corresponds to continuous line and numerical solution to open circles.

domain, the concentration profile in the fluid phase can be found through integrating Eq. (5), at steady state, with two Dirichlet boundary conditions, $C^* = C_s^*|_{r^* = r_p^*}$ and $C^* = C_\infty^*|_{r^* = r_B^*}$. The concentration profile due to diffusion in a bounded spherical domain of radius r_B^*, Eq. (18), is used to determined the mass transfer coefficient and the particle surface concentration.

$$C^*(r^*) = \frac{r_p^* r_B^*}{\left(r_p^* - r_B^*\right) r}\left(C_\infty^* - C_s^*\right) + \frac{C_s^* r_p^* - C_\infty^* r_B^*}{r_p^* - r_B^*} \qquad (18)$$

To validate our numerical simulations, we use the surface concentration C_s^* provided by Eq. (9). We compare the dimensionless concentration profiles in the particle, i.e., Eq. (2) and in the fluid phase, i.e., Eq. (18) to our computed profiles. We consider two different cases. In the first case, we set the Thiele modulus to $\phi = 20$ and the diffusion ratio to $\gamma = 10$ and plot analytical and computed solutions in Fig. 4. In the second case, we set the Thiele modulus to $\phi = 20$ and the diffusion ratio to $\gamma = 0.1$ and plot analytical and computed solutions in Fig. 5. A very good agreement has been obtained between the analytical predictions and the numerical simulations.

Then, we vary the Thiele modulus ϕ from 0 to 40 and we plot the surface concentration for $Re = 0$ corresponding to external diffusion only ($Sh = 2$) in Fig. 6. Our computed results show again a very good agreement with the analytical prediction.

3.2. Fully coupled model and simulations

In this section the hydrodynamics is added to the problem and the particle experiences external convection with a uniform inlet velocity as sketched in Fig. 7, i.e., at Reynolds number $Re \neq 0$ (see Fig. 8).

The problem is treated as two coupled systems: an external problem involving convection diffusion and an internal problem involving diffusion reaction. In this case, the problem is governed by the following four dimensionless numbers: the Thiele modulus ϕ and the diffusion coefficient ratio γ for diffusion reaction, and the Reynolds number Re and the Schmidt Sc for convection diffusion.

The ranges of dimensional physical parameters generally encountered in gas solid and liquid solid industrial applications are summarized in Table 1. Liquids are typically hydrocarbons such as Heptane, Decane, or Hexadecane. Gases are a mixture of
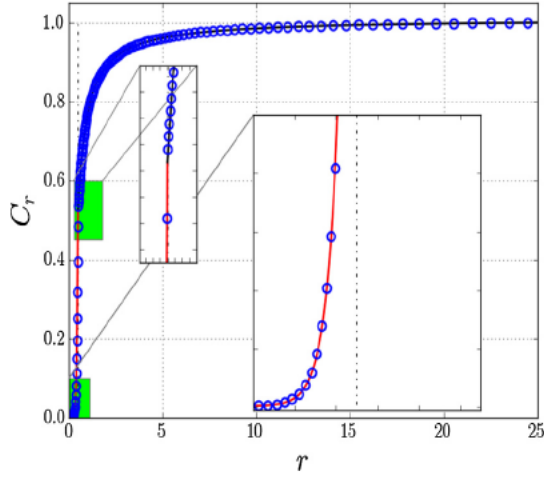
Fig. 5. Concentration profile as function of dimensionless radius for γ 0.1 and ϕ 20. Inset stands for a zoom on the particle surface (r^*/r_p^* 1). Particle interface is represented by vertical dashed-doted line, analytical solution corresponds to continuous line and numerical solution by open circles.
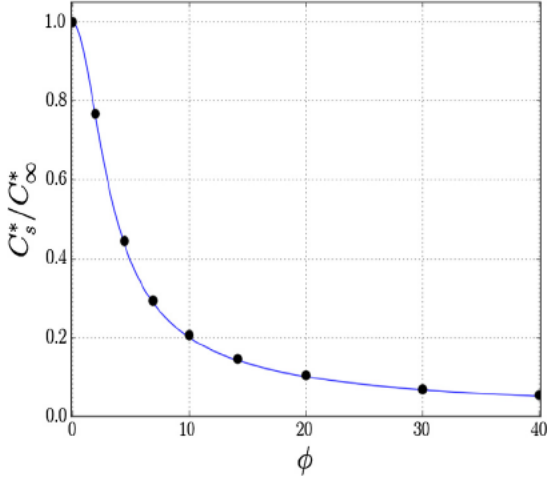

Fig. 6. Surface concentration as function of Thiele modulus at steady state in the diffusive regime. Continuous line and black circles correspond to analytical solution and simulation results respectively.


Fig. 7. Schematic diagram of the flow configuration and physical properties. The numerical domain size is $L_x^* \times L_y^*$ $100 r_p^* \times 100 r_p^*$.

hydrogen gas and hydrocarbons. According to this table, the corresponding ranges of dimensionless numbers are: $\gamma \in [0.01, 1]$, $\phi \in [0.02, 6]$, $Re \in [0, 200]$, and $Sc \in [1, 1000]$.
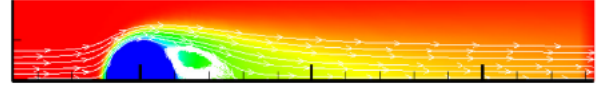
In this case, fluid flows with an imposed inlet concentration and reacts within the catalyst particle.
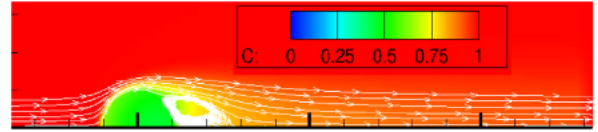
(a) $\phi = 2$, $Re = 100$, $Sc = 1$ and $\gamma = 10$.
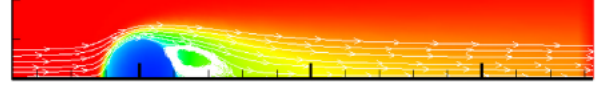
(b) $\phi = 6$, $Re = 100$, $Sc = 1$ and $\gamma = 10$.

(c) $\phi = 200$, $Re = 100$, $Sc = 1$ and $\gamma = 10$.

Fig. 8. Concentration spatial distribution for (a) slow reaction (b) intermediate, and (c) fast reactions at Reynolds number Re 100.

Table 1
Physical properties of industrial gas-solid and liquid-solid reactive particulate systems.

Parameter	Catalyst particle	Liquid	Gas
D^* (m^2 s^1)	$10^{6} - 10^{10}$	$\sim 10^{9}$	$10^{6} - 10^{5}$
r_p^* (mm)	1–5	–	–
k_s^* (s^1)	$10^{6} - 10$;	–	–
u_f^* (cm s^1)	–	1–2	0.2–20
μ_f^* (mPa s)	–	0.386–0.92	~ 0.9
ρ_f^* (kg m^3)	–	695–770	~ 100

According to reaction kinetics, three regimes can be identified as follows.

(1) If the reaction rate is sufficiently slow compared to the diffusion rate ($\phi \ll 1$), the concentration at the catalyst particle surface is the same as the inlet fluid concentration. This regime is referred to as reaction limited.

(2) When the reaction rate is extremely fast ($\phi \gg 1$) compared to diffusion rate, the catalyst surface concentration approaches zero and the process is controlled by mass transfer resistance.

(3) The third regime is when none of the two previous regimes is predominant and the catalyst surface concentration is unknown. The aim of our work is to propose a model covering the three regimes. The model for the prediction of the mean surface concentration is presented in Eq. (12) and compared to numerical simulations to test the validity of the range of physical parameters listed in Table 1.

The external Sherwood number is evaluated from the correlation of Feng and Michaelides (2000) given in Eq. (19). This correlation corresponds to a purely mass transfer controlled system and is valid for Peclet and Reynolds numbers above 10. It exhibits the best agreement with our numerical results for convective diffusive mass transfer as shown in Fig. 3. Note that for a convection free, i.e., purely diffusive, problem the solution is analytical as the external Sherwood number has an exact value 2 which unfortunately is not the limit of the correlation towards low Peclet and Reynolds numbers.

$$Sh \quad 0.922 + Pe^{1/3} + 0.1 Re^{1/3} Pe^{1/3} \tag{19}$$

In the presence of chemical reaction, the mean surface concentration $\overline{C_s^*}$ has been numerically evaluated according to Eq. (20) and computed results are compared with the model.

$$\overline{C_s^*} = \frac{1}{2}\int_0^\pi C^*(r^* = r_p^*,\theta)\sin(\theta)d\theta \qquad (20)$$

First, we set the Schmidt number to $Sc = 1$ and the diffusion coefficient ratio to $\gamma = 0.1$. We plot in Fig. 9 the mean surface concentration as a function of the Reynolds number from 20 to 200 for 3 values of the Thiele modulus $\phi = 60$, $\phi = 200$ and $\phi = 6 \cdot 10^4$. Second, we set the Schmidt number to $Sc = 10$ and the diffusion coefficient ratio to $\gamma = 0.1$. We plot in Fig. 10 the mean surface concentration as a function of the Reynolds number from 20 to 200 for 3 values of the Thiele modulus $\phi = 200$, $\phi = 632$ and $\phi = 2 \cdot 10^4$. In all cases, the surface concentration is observed to be decreasing with the increase of Thiele modulus at constant Reynolds number and increasing with the increase of the Reynolds number at constant Thiele modulus. In general, our computed results match well our proposed model (12).

The spatial distributions of concentration are shown in Fig. 11 for four Thiele moduli. (a) Represents a slow reaction rate or kinetics limited system with $\phi = 2$, (e) represents a mass transfer controlled system for Thiele modulus $\phi = 2 \cdot 10^4$, (b), (c) and (d) represent a system that is neither reaction nor mass transfer controlled.

The concentration profiles along the arc length have been plotted in Fig. 12. In case A, the surface concentration is constant and is equal to that of inlet fluid. In case E, the surface concentration is also constant and it approaches zero. In cases B, C and D the systems are neither controlled by kinetics nor by mass transfer and the surface concentration is non uniform and attains a minimum near the separation angle θ_s of the wake. These spatial variations of the surface concentration may induce non uniformity of the local mass flux. We investigate the variations of the local dimensionless flux $2\pi \frac{\partial C}{\partial r} r^2 \sin(\theta)d\theta$ along the arc length θ. In Fig. 13, the local flux has been normalized by its average for the cases A, C and E of Fig. 12. For case A, the concentration gradient normal to the particle surface is almost constant while the surface concentration is equal to the bulk concentration. The local flux of mass follows the variation of

Fig. 10. Mean surface concentration as function of Reynolds number at steady state, $Sc = 10$, $\gamma = 0.1$ and 3 Thiele moduli. Case 1, $\phi = 200$, model represented by dashed-doted line and simulations by blue disks. Case 2, $\phi = 632$, model represented by red line and simulations by red triangles. Case 3, $\phi = 2 \cdot 10^4$, model represented by dashed-doted green line and simulations by green squares. The error bars correspond to minimum and maximum concentration values along θ. (For interpretation of the references to color in this figure legend, the reader is referred to the web version of this article.)

the sine function corresponding to local element of surface (zero at the poles and maximum in the equatorial plane). For cases C and E, the gradient of concentration varies along θ in combination with the elementary surface yielding non monotonous variation of the local mass flux. Mass flux is enhanced in the region of strong effect of convection (between $\pi/4$ in the front of the particle and the equatorial plane) while chemical reaction yields lower concentration at the rear of the particle. This can be observed in Fig. 12. All those non uniformities of concentration and mass flux distributions cancel out yielding good accuracy of our simple modeling based on uniform surface concentration. This is supported by Fig. 14 showing that the concentration profiles for any angle within the particle is very close to the analytic Thiele profile when the concentration is made dimensionless by the local surface concentration $C_s^*(\theta)$.

We focus now on the mean volume concentration within the particle which can be determined numerically by integrating the spatial distribution of concentration:

$$\overline{C_v^*} = \frac{6}{\pi d_p^{*3}}\int_0^{2\pi}\int_0^\pi\int_0^{r_p^*} C(r^*,\theta)\sin(\theta)r^{*2}d\varphi d\theta dr^* \qquad (21)$$

When the mean surface concentration $\overline{C_s^*}$ is known, the mean volume concentration can be evaluated analytically as:

$$\overline{C_v^*} = \eta\overline{C_s^*} = \frac{6\overline{C_s^*}}{\phi}\left(\frac{1}{tanh(\phi/2)} - \frac{2}{\phi}\right) \qquad (22)$$

$\overline{C_s^*}$ is estimated by the model Eq. (12) and therefore the mean volume concentration can be written as follows:

$$\overline{C_v^*} = \frac{3C_\infty^*}{1+\frac{2\gamma}{Sh}\left(\frac{\phi/2}{tanh(\phi/2)}-1\right)}\left(\frac{2}{\phi tanh(\phi/2)}-\frac{4}{\phi^2}\right) \qquad (23)$$

The molar flux towards the particle at steady state is balanced by internal reaction. We can define the factor of enhancement in Eq. (24) that measures the effect of the chemical reaction to a reference case without any resistance to transfer. This factor for a catalyst particle is defined as the internal rate of reaction inside the particle, to the rate that would be attained with a particle at uniform concentration C_∞^* corresponding to maximum
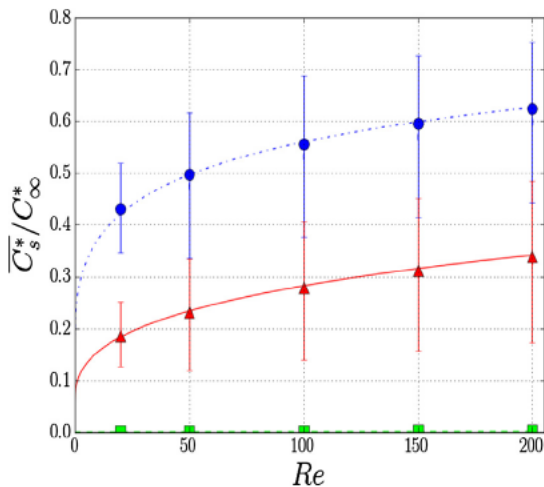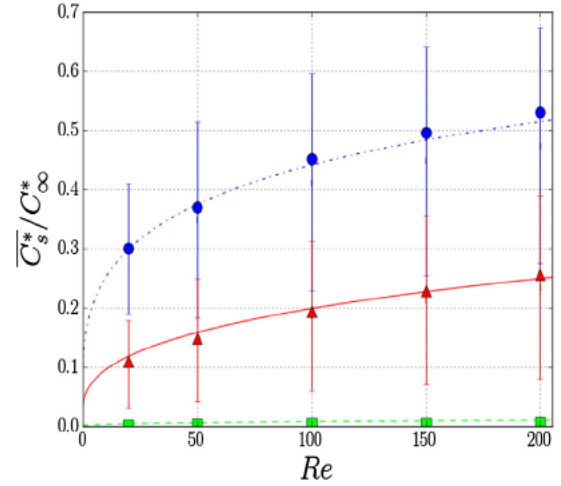

Fig. 9. Mean surface concentration as function of Reynolds number at steady state, $Sc = 1$, $\gamma = 0.1$ and three Thiele moduli. Case 1, $\phi = 60$, model represented by dashed-doted line and simulations by blue disks. Case 2, $\phi = 200$, model represented by red line and simulations by red triangles. Case 3, $\phi = 6 \cdot 10^4$, model represented by dashed-doted green line and simulations by green squares. The error bars correspond to minimum and maximum concentration values along θ. (For interpretation of the references to color in this figure legend, the reader is referred to the web version of this article.)
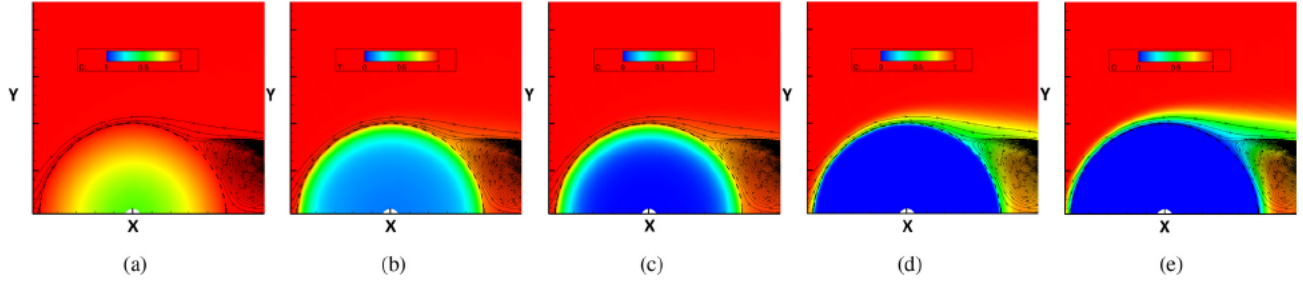
Fig. 11. Spatial distribution of concentration at Reynolds number $Re = 100$, $Sc = 10$ and $\gamma = 0.1$ for different Thiele moduli. (a) $\phi = 2$, (b) $\phi = 20$, (c) $\phi = 200$, (d) $\phi = 632$ and (e) $\phi = 2 \cdot 10^4$.
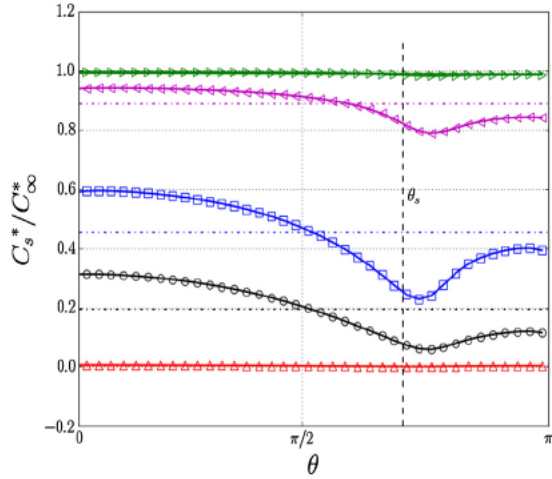

Fig. 12. Surface concentration variation along the arc length at Reynolds number $Re = 100$, $Sc = 10$ and $\gamma = 0.1$ for different Thiele moduli. Case A, $\phi = 2$ represented by continuous line and right triangles. Case B, $\phi = 20$ represented by continuous line and left triangles. Case C, $\phi = 200$ represented by continuous line and squares. Case D, $\phi = 632$, represented by continuous line and circles. Case E $\phi = 2 \cdot 10^4$, represented by continuous line and up-down triangles. Horizontal dashed doted lines correspond to mean surface concentration $\overline{C_s^*}$ and vertical dashed line locates the separation angle θ_s of the wake streamlines.
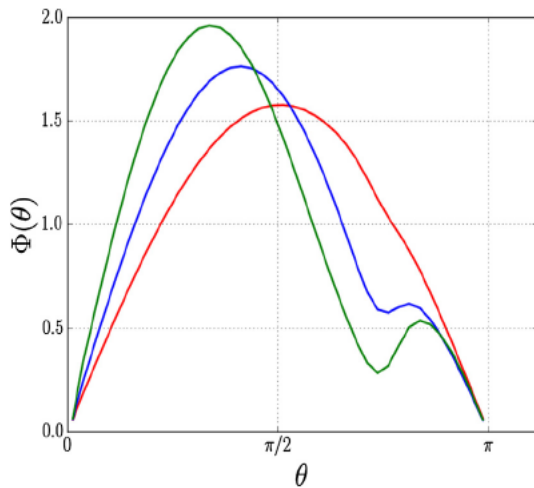

Fig. 13. Local dimensionless mass flux along the arc length at Reynolds number $Re = 100$, $Sc = 10$ and $\gamma = 0.1$ for different Thiele moduli. Case A, $\phi = 10$ represented by red line. Case C, $\phi = 200$ represented by blue line. Case E, $\phi = 2 \cdot 10^4$ represented by green line. (For interpretation of the references to color in this figure legend, the reader is referred to the web version of this article.)

consumption rate. For a reactive catalyst particle experiencing an external convective diffusive stream, the enhancement factor can be expressed as:

$$\widetilde{E} = \frac{\int_0^{2\pi} \int_0^\pi \int_0^{\vec{r}_p} k_s^* C^*(r^*, \theta) \sin(\theta) r^{*2} d\varphi d\theta dr^*}{k_s^* \frac{\pi d_p^{*3}}{6} C_\infty^*}$$

$$= \frac{3(\phi/2 - \tanh(\phi/2))}{\frac{\phi^2}{4} \tanh(\phi/2) \left[1 + \frac{2\gamma}{Sh}\left(\frac{\phi/2}{\tanh(\phi/2)} - 1\right)\right]} \quad (24)$$

Depending on reaction kinetics, the enhancement factor has two asymptotic limits. For very slow reaction, i.e $\phi \ll 1$, the process is kinetics controlled and the catalyst surface concentration is equal to fluid inlet concentration, therefore $\widetilde{E} \to 1$. For fast reaction, i.e $\phi \gg 1$, the process is limited by mass transfer and the surface concentration approaches zero, in this case $\widetilde{E} \to 1/\left(1 + \frac{\gamma\phi^2}{6Sh}\right)$ which is lower than one and may be very small for $\phi^2 \gamma/Sh \gg 1$.

We compare the enhancement factor $\widetilde{E} = \eta \frac{\overline{C_s^*}}{C_\infty^*} = \frac{\overline{C_v^*}}{C_\infty^*}$ from the numerical simulations to the predictions of the model. The results shown in Figs. 15 and 16 correspond to cases presented for mean surface concentration in Figs. 9 and 10, respectively. A slight over estimation of the model occurs at high Reynolds number and $Sc = 10$.

4. Transient evolution

4.1. Unsteady mass balance

The aim of our work is to establish a model for a mass transfer coefficient which accounts for the effect of a first order irreversible reaction along with convection and diffusion. The model depends on mean volume concentration instead of mean surface concentration, and can be used as a closure law in meso scale simulations such as DEM CFD, where mean quantities are known at particle scale. In the DEM CFD framework, the particle concentration is a Lagrangian quantity the evolution of which is integrated over time along the trajectory. Therefore, there is no resolution of the interior of the particle assuming homogeneous concentration. The purpose of our model is indeed to account for internal mass diffusion and reaction due to the coupling of internal and external transport phenomena corresponding to non uniform concentration distributions that cannot be resolved in DEM CFD (particles are much smaller than the mesh cells). Thus, the mass flux balance is expressed as:

$$\frac{\pi d_p^{*3}}{6} \frac{d\overline{C_v^*}}{dt^*} = 4\pi r_p^{*2} h^* \left(\overline{C_v^*} - C_\infty^*\right) - \frac{\pi d_p^{*3}}{6} k_s \overline{C_v^*} \quad (25)$$

Mass conservation yields

$$4\pi r_p^{*2} h^* \left(\overline{C_v^*} - C_\infty^*\right) = 4\pi r_p^{*2} k_f^* \left(\overline{C_s^*} - C_\infty^*\right) \quad (26)$$

where k_f^* is the external mass transfer coefficient referring to concentration difference $\Delta C^* = \left(\overline{C_s^*} - C_\infty^*\right)$, and h^* is the overall mass transfer coefficient that accounts for internal and external effects
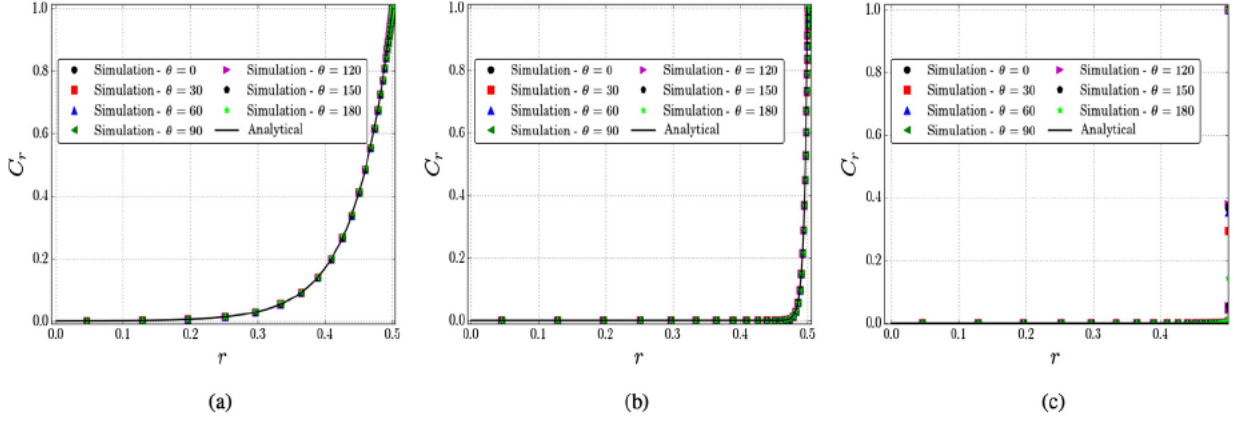
Fig. 14. Concentration profiles C_r inside the particle normalized by the local surface concentration for different angles θ for the three cases that correspond to $Re = 100$, $Sc = 10$ and $\gamma = 0.1$ for different Thiele moduli. (a) Corresponds to Case B, $\phi = 20$. (b) Corresponds to Case C, $\phi = 200$. (c) Corresponds to Case E, $\phi = 2 \cdot 10^4$.
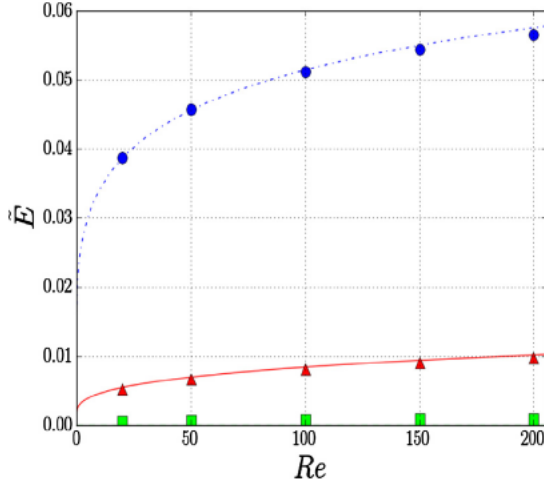

Fig. 15. Enhancement factor as function of Reynolds number at steady state, $Sc = 1$, $\gamma = 0.1$ and 3 Thiele moduli. Case 1, $\phi = 60$, model represented by dashed-doted line and simulations by blue disks. Case 2, $\phi = 200$, model represented by red line and simulations by red triangles. Case 3, $\phi = 6 \cdot 10^4$ model represented by dashed-doted green line and simulations by green squares. (For interpretation of the references to color in this figure legend, the reader is referred to the web version of this article.)
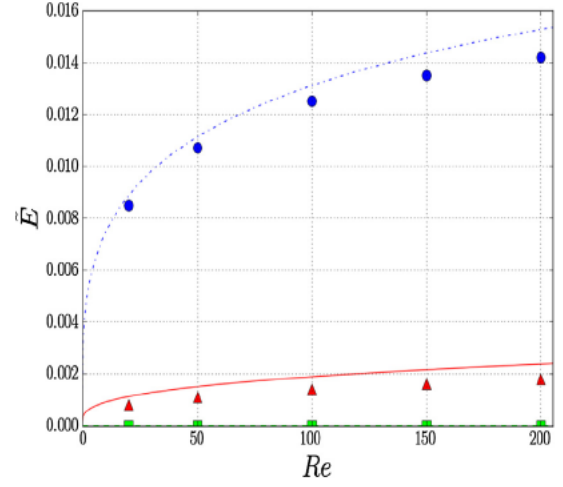

Fig. 16. Enhancement factor as function of Reynolds number at steady state, $Sc = 10$, $\gamma = 0.1$ and 3 Thiele moduli. Case 1, $\phi = 200$, model represented by dashed-doted line and simulations by blue disks. Case 2, $\phi = 632$, model represented by red line and simulations by red triangles. Case 3, $\phi = 6 \cdot 10^4$ model represented by dashed-doted green line and simulations by green squares. (For interpretation of the references to color in this figure legend, the reader is referred to the web version of this article.)

and refers to the mean catalyst particle concentration, $\Delta \overline{C^*} = \left(\overline{C^*_v} - C^*_\infty \right)$. Thus, the mass transfer coefficient including the effect of chemical reaction can be obtained as:

$$h^* = k_f^* \frac{\Delta C^*}{\Delta \overline{C^*}} = k_f^* \frac{1 - \tilde{E}/\eta}{1 - \tilde{E}} \tag{27}$$

which can be written in a dimensionless form as an effective Sherwood number $Sh = \frac{h^* d_p^*}{D_f^*}$.

Substituting the effectiveness and enhancement factors, $\tilde{Sh}(Re, Sc, \phi, \gamma)$ can be written as:

$$\tilde{Sh}(Re, Sc, \phi, \gamma) = \frac{Sh(Re, Sc)}{\frac{Sh(Re, Sc)}{2\gamma} \left[\frac{tanh(\phi/2)}{\phi/2} - \frac{tanh(\phi/2)}{\phi^2} - \frac{12}{\phi^2} \right] + 1} \tag{28}$$

This is equivalent to the additivity rule, i.e., the summation of the resistances to transfer:

$$\frac{1}{\tilde{Sh}} = \frac{1}{2\gamma} \left[\frac{tanh(\phi/2)}{\phi/2 \ tanh(\phi/2)} - \frac{12}{\phi^2} \right] + \frac{1}{Sh} \tag{29}$$

The model presented in Eq. (29) has two asymptotic limits. For very fast reaction, i.e when Thiele modulus $\phi \to \infty$, the term $\left[\frac{tanh(\phi/2)}{\phi/2 \ tanh(\phi/2)} - \frac{12}{\phi^2} \right] \to 0$ and therefore $\tilde{Sh} \to Sh$. In this case the system is controlled by mass transfer. For very slow reaction, i.e Thiele modulus $\phi \to 0$, the term $\left[\frac{tanh(\phi/2)}{\phi/2 \ tanh(\phi/2)} - \frac{12}{\phi^2} \right] \to \infty$ yielding $\tilde{Sh} \to 0$. In this case, mass transfer is controlled by internal reaction kinetics. Between the asymptotic regimes, the system is neither mass transfer nor kinetics controlled. Numerical simulations have been performed and $\tilde{Sh}$ has been calculated numerically according to Eq. (30) to be compared to our model given by Eq. (28).

$$\tilde{Sh}_{sim} = \frac{d_p^*}{2 \left(C^*_\infty - \overline{C^*_v} \right)} \int_0^\pi \left(\frac{\partial C^*(r^*, \theta)}{\partial r^*} \right)_{r^* = r_p^*} sin(\theta) d\theta \tag{30}$$

We present two sets of simulation to validate the model. In set 1, we set $Sc = 1$, $\gamma = 0.1$, consider three Thiele moduli: [$\phi = 60$, Case 1], [$\phi = 200$, Case 2] and [$\phi = 6 \cdot 10^4$, Case 3], and vary Re from 20 to 200. In set 2, we set $Sc = 10$, $\gamma = 0.1$, consider three

Thiele moduli: $[\phi = 200,\ \text{Case 1}]$, $[\phi = 632,\ \text{Case 2}]$ and $[\phi = 2 \cdot 10^4$, Case 3], and vary Re from 20 to 200. Computed results from sets 1 and 2 are plotted in Figs. 17 and 18, respectively. They show a very good agreement with the predictions of our model.

4.2. Transient evolution of catalyst bead concentration

We consider here a particle of mean initial volume concentration $\overline{C_v^*}(t^* = 0) = 0$, placed in a steady stream of uniform concentration C_∞^*. A first order reaction is taking place within the particle. The temporal evolution of the mean volume concentration within the particle is described by Eq. (25), which can be written in a dimensionless form as follows:
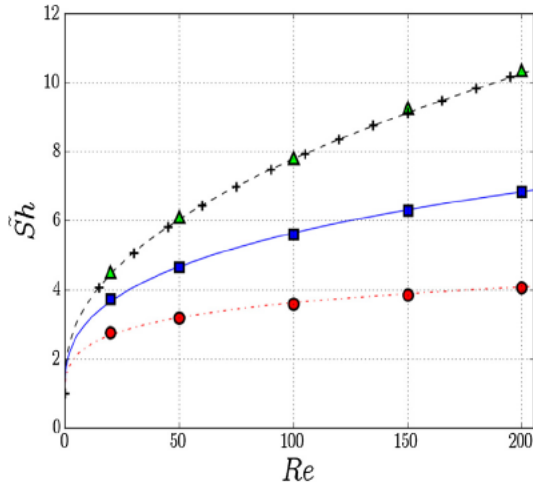

Fig. 17. Sh as function of Reynolds number at steady state, $Sc = 1$, $\gamma = 0.1$ and three Thiele moduli. Case 1, $\phi = 60$, model represented by red dashed-doted line and simulation results by disks. Case 2, $\phi = 200$, model represented by blue continuous line and simulation results by squares. Case 3, $\phi = 6 \cdot 10^4$, model represented by red dashed line and simulation results by triangles. The + markers correspond to the correlation of Feng and Michaelides (2000). (For interpretation of the references to color in this figure legend, the reader is referred to the web version of this article.)
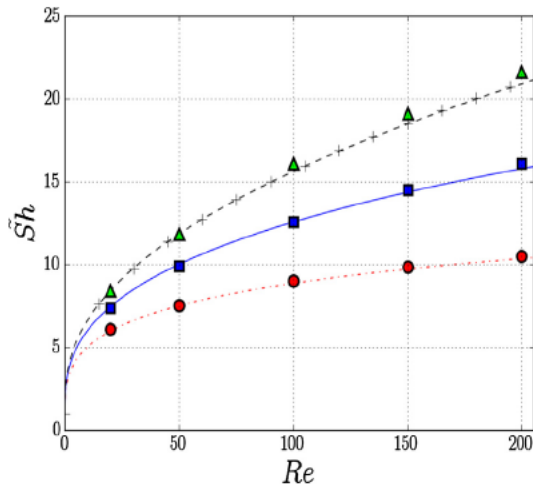

Fig. 18. Sh as function of Reynolds number at steady state, $Sc = 10$, $\gamma = 0.1$ and three Thiele moduli. Case 1, $\phi = 200$, model represented by red dashed-doted line and simulation results by disks. Case 2, $\phi = 632$, model represented by blue continuous line and simulation results by squares. Case 3, $\phi = 2 \cdot 10^4$, model represented by red dashed line and simulation results by triangles. The + markers correspond to the correlation of Feng and Michaelides (2000). (For interpretation of the references to color in this figure legend, the reader is referred to the web version of this article.)

$$\frac{d\overline{C_v}}{dt} = \left(\overline{C_v} - 1\right) - k_s \overline{C_v} \tag{31}$$

with $\overline{C_v} = \overline{C_v^*}/C_\infty^*$ and $k_s = k_s^* d_p^*/6h^*$. At steady state, $\frac{d\overline{C}}{dt} = 0$, which yields the mean volume concentration as:

$$\overline{C_f} = \left(1 + \frac{k_s^* d_p^*}{6h^*}\right)^{-1} = \left(1 + \frac{\gamma \phi^2}{6\tilde{S}h}\right)^{-1} \tag{32}$$

$\overline{C_f}$ is equal to the mean volume concentration found by the steady balance in Eq. (23) normalized by C_∞. The analytic solution of Eq. (31) is:

$$\overline{C_v}(t) = \overline{C_f}\left(1 - \exp\left(-\frac{t}{\overline{C_f}}\right)\right) \tag{33}$$
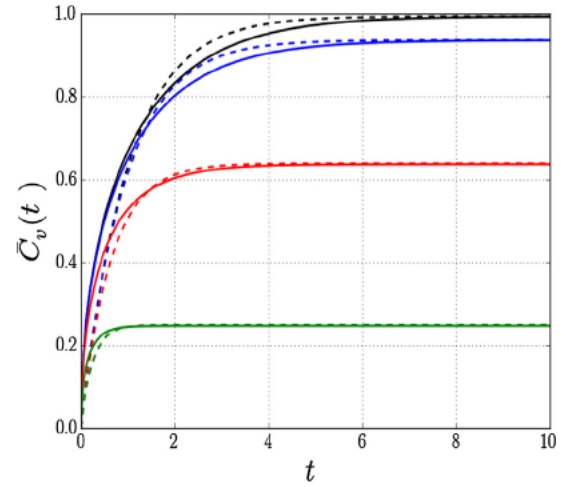

Fig. 19. Temporal evolution of the dimensionless mean volume concentration, model comparison with simulation for $Re = 200$, $Sc = 10$, $\gamma = 0.1$ and four Thiele moduli. Model represented by dashed and simulation by continuous lines, respectively. Case1, $\phi = 0.6$ – black color. Case 2, $\phi = 2$ – blue color. Case 3, $\phi = 6$ – red color. Case 4, $\phi = 20$ – green color. (For interpretation of the references to color in this figure legend, the reader is referred to the web version of this article.)

Fig. 20. Temporal evolution of the dimensionless mean volume concentration, model comparison with simulation for $Re = 100$, $Sc = 1$, $\gamma = 0.1$ and four Thiele moduli. Model represented by dashed and simulation by continuous lines, respectively. Case1, $\phi = 0.88$ – black color. Case 2, $\phi = 2.8$ – blue color. Case 3, $\phi = 8.8$ – red color. Case 4, $\phi = 28.2$ – green color. (For interpretation of the references to color in this figure legend, the reader is referred to the web version of this article.)
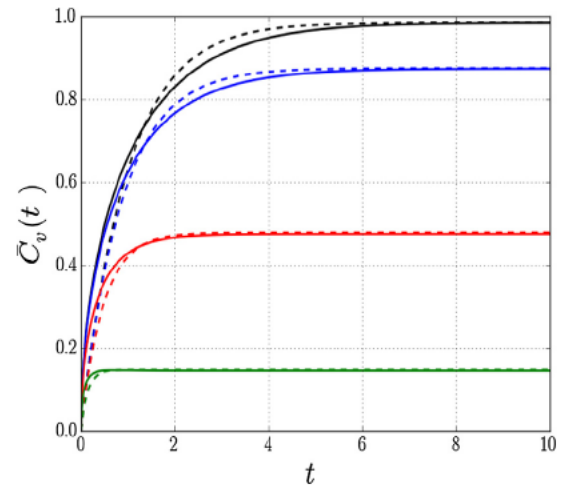
where $t = t^*/\tau^*$ is the dimensionless time and $\tau^* = d_p^*/6h^*$ with $h^* = ShD_f^*/d_p^*$ is the mass transfer coefficient given by Eq. (28).

We compare the unsteady predictions of the model to computed results through two sets of simulations (each of them at a fixed Reynolds number). In set 1, we set $Re = 200$, $Sc = 10$, $\gamma = 0.1$ and vary ϕ from 0.6 to 20. We plot the results in Fig. 19. In set 2, we set $Re = 100$, $Sc = 1$, $\gamma = 0.1$ and vary ϕ from 0.88 to 28.2. We plot the results in Fig. 20. The model has shown its ability to predict the characteristic time of the mean concentration evolution and a good agreement has been observed between the model and the numerical simulations, although we assumed the mass transfer rate to be constant. The transient model allows to estimate the time needed for a catalyst bead to reach its steady mean concentration. Typically, the characteristic time is less than a second for a gas-solid system and around tens of seconds for liquid-solid systems.

5. Conclusion and future work

We investigated mass transfer for a system composed of an isolated solid spherical catalyst particle placed within a fluid stream. Reactant diffuses from the fluid phase to the solid phase where a first order irreversible chemical reaction takes place. The problem is treated by coupling external convection-diffusion in the fluid phase to diffusion-reaction in the solid phase through appropriate boundary conditions, namely continuity of concentration and continuity of flux at the particle interface. We solved the whole problem in two ways: (i) through boundary fitted numerical simulations of the full set of equations and (ii) through a simple semi-analytical approach that couples a correlation for the external transfer to an analytical solution of the internal diffusion-reaction equation. The interplay between the different transport phenomena can be quantified through an effective Sherwood number assuming steady state. The prediction of this effective Sherwood number in such systems has a key role in terms of modeling while it allows to estimate the equilibrium internal mean concentration of the particle without using the determination of the surface concentration (unknown in such situations).

The model has been validated step by step. To start with, a diffusion-reaction problem has been considered in the absence of convection in the fluid phase. In this case, the external Sherwood number has an analytical solution $Sh = 2$. This allows to find the analytical solution for the surface concentration at steady state and to test the accuracy of our numerical simulations. Then, the particle was exposed to an external fluid stream with an inlet concentration C_∞. In this case, the mean surface concentration has been modeled using a classical correlation for the mass transfer coefficient. Our model was compared with numerical simulations over a wide range of dimensionless parameters. Both mean surface and mean volume concentrations predicted by our model showed a satisfactory agreement with numerical simulation results. This satisfactory agreement also support that notion that the assumptions of the model are appropriate.

An expression for the mass tranfer coefficient that accounts for internal and external effects in the system has been proposed, via general mass balance for the system and equivalently using additivity rule of resistances to mass transfer. It has also been validated through comparison with numerical simulations. The major result of our study is that our simple model based on decoupled treatment of internal and external mass transfer gives very accurate results. The asymptotic limits of the model have been analyzed and are in accordance with general expectations for slow and fast reaction rates. Finally, the unsteady response on the system has been tested. A model that predicts the time evolution of the mean volume concentration has been established. It is in a very good agreement with unsteady simulations results.

Possible extensions of this model are as follows. To be useful for engineering applications, such model should include the effect of neighboring particles corresponding to situations at higher solid volume fraction as a fixed bed or a fluidized bed. The effect of the particle volume fraction can be investigated with a particle resolved numerical approach that solves both internal and external mass balances either with a boundary fitted mesh (Partopour and Dixon, 2017a) or with an immersed boundary/ghost fluid method (Shao et al., 2012). Another extension of our work is to address more complex chemical reactions as, e.g., different reaction kinetics, second order reactions or multiple reactions with additional species.

Conflict of interest

The authors declared that there is no conflict of interest.

Acknowledgments

References

Baruah, D., Baruah, D., Hazarika, M., 2017. Artificial neural network based modeling of biomass gasification in fixed bed downdraft gasifiers. Biomass Bioenergy 98, 264–271. https://doi.org/10.1016/j.biombioe.2017.01.029 <http://www.sciencedirect.com/science/article/pii/S0961953417300569>.

Bird, R.B., Stewart, W.E., Lightfoot, E.N., Klingenberg, D.J., 2015. Transport Phenomena. second ed. Wiley.

Bohn, C., Scott, S.A., Dennis, J.S., Müller, C., 2012. Validation of a lattice boltzmann model for gas-solid reactions with experiments. J. Comput. Phys. 231, 5334–5350.

Calmet, I., Magnaudet, J., 1997. Large-eddy simulation of high-schmidt number mass transfer in a turbulent channel flow. Phys. Fluids 9, 438–455.

Clift, R., Grace, J.R., Weber, M.E., 2005. Bubbles, Drops, and Particles. Courier Corporation.

Dierich, F., Richter, A., Nikrityuk, P., 2018. A fixed-grid model to track the interface and porosity of a chemically reacting moving char particle. Chem. Eng. Sci. 175, 296–305.

Dixon, A.G., Taskin, M.E., Nijemeisland, M., Stitt, E.H., 2010. Cfd method to couple three-dimensional transport and reaction inside catalyst particles to the fixed bed flow field. Ind. Eng. Chem. Res. 49, 9012–9025.

Feng, Z.G., Michaelides, E.E., 2000. A numerical study on the transient heat transfer from a sphere at high reynolds and peclet numbers. Int. J. Heat Mass Transfer 43, 219–229.

Gunn, D., 1978. Transfer of heat or mass to particles in fixed and fluidised beds. Int. J. Heat Mass Transfer 21, 467–476.

Ismail, T.M., El-Salam, M.A., Monteiro, E., Rouboa, A., 2017. Fluid dynamics model on fluidized bed gasifier using agro-industrial biomass as fuel. Waste Manage. doi: https://doi.org/10.1016/j.wasman.2017.06.018. <http://www.sciencedirect.com/science/article/pii/S0956053X17304592>.

Jarullah, A.T., Awad, N.A., Mujtaba, I.M., 2017. Optimal design and operation of an industrial fluidized catalytic cracking reactor. Fuel 206, 657–674.

Juncu, G., 2001. The influence of the henry number on the conjugate mass transfer from a sphere. Heat Mass Transfer 37, 519–530.

Juncu, G., 2002. The influence of the henry number on the conjugate mass transfer from a sphere: II – Mass transfer accompanied by a first-order chemical reaction. Heat Mass Transfer 38, 523–534.

Kleinman, L.S., Reed, X.J., 1995. Interphase mass transfer from bubbles, drops, and solid spheres: diffusional transport enhanced by external chemical reaction. Ind. Eng. Chem. Res. 34, 3621–3631.

Losey, M.W., Schmidt, M.A., Jensen, K.F., 2001. Microfabricated multiphase packed-bed reactors: characterization of mass transfer and reactions. Ind. Eng. Chem. Res. 40, 2555–2562.

Lu, J., Das, S., Peters, E., Kuipers, J., 2018. Direct numerical simulation of fluid flow and mass transfer in dense fluid-particle systems with surface reactions. Chem. Eng. Sci. 176, 1–18.

Magnaudet, J., Rivero, M., Fabre, J., 1995. Accelerated flows past a rigid sphere or a spherical bubble. Part 1. Steady straining flow. J. Fluid Mech. 284, 97–135.

Mikulandrić, R., Böhning, D., Böhme, R., Helsen, L., Beckmann, 2016. Dynamic modelling of biomass gasification in a co-current fixed bed gasifier. Energy Convers. Manage. 125, 264–276.

Neves, D., Matos, A., Tarelho, L., Thunman, H., Larsson, A., Seemann, M., 2017. Volatile gases from biomass pyrolysis under conditions relevant for fluidized bed gasifiers. J. Anal. Appl. Pyrol. 127, 57–67. https://doi.org/10.1016/j.jaap.2017.09.002 <http://www.sciencedirect.com/science/article/pii/S0165237017305090>.

Partopour, B., Dixon, A., 2017a. An integrated workflow for resolved-particle packed bed models with complex particle shapes. Powder Technol. 322, 258–272.

Partopour, B., Dixon, A.G., 2017b. Resolved-pore simulation of co oxidation on rh/al2o3 in a catalyst layer. ChemEngineering 2, 2.

Piché, S., Grandjean, B.P., Iliuta, I., Larachi, F., 2001. Interfacial mass transfer in randomly packed towers: a confident correlation for environmental applications. Environ. Sci. Technol. 35, 4817–4822.

Pigeonneau, F., Perrodin, M., Climent, E., 2014. Mass-transfer enhancement by a reversible chemical reaction across the interface of a bubble rising under stokes flow. AIChE J. 60, 3376–3388.

Ranz, W., Marshall, W., et al., 1952. Evaporation from drops. Chem. Eng. Prog. 48, 141–146.

Rossetti, I., 2017. Continuous flow (micro-) reactors for heterogeneously catalyzed reactions: Main design and modelling issues. Catal. Today.

Ruckenstein, E., Dang, V.D., Gill, W.N., 1971. Mass transfer with chemical reaction from spherical one or two component bubbles or drops. Chem. Eng. Sci. 26, 647–668.

Shao, X., Shi, Y., Yu, Z., 2012. Combination of the fictitious domain method and the sharp interface method for direct numerical simulation of particulate flows with heat transfer. Int. J. Heat Mass Transfer 55, 6775–6785.

Sherwood, T., Wei, J., 1957. Interfacial phenomena in liquid extraction. Ind. Eng. Chem. 49, 1030–1034.

Wakao, N., Funazkri, T., 1978. Effect of fluid dispersion coefficients on particle-to-fluid mass transfer coefficients in packed beds: correlation of sherwood numbers. Chem. Eng. Sci. 33, 1375–1384.

Wehinger, G.D., Klippel, F., Kraume, M., 2017. Modeling pore processes for particle-resolved cfd simulations of catalytic fixed-bed reactors. Comput. Chem. Eng. 101, 11–22.

Whitaker, S., 1972. Forced convection heat transfer correlations for flow in pipes, past flat plates, single cylinders, single spheres, and for flow in packed beds and tube bundles. AIChE J. 18, 361–371.